DTU Library

Anisotropic yield surfaces of additively manufactured metals simulated with crystal plasticity

Somlo, K.; Frodal, B.H.; Funch, C.V.; Poulios, K.; Winther, G.; Hopperstad, O.S.; Børvik, T.; Niordson, C.F.

Published in:
European Journal of Mechanics A - Solids

Link to article, DOI:
10.1016/j.euromechsol.2022.104506

Publication date:
2022

Document Version
Peer reviewed version

Journal Pre-proof

Anisotropic yield surfaces of additively manufactured metals simulated with crystal plasticity

K. Somlo, B.H. Frodal, C.V. Funch, K. Poulios, G. Winther, O.S. Hopperstad, T. Børvik, C.F. Niordson

PII: S0997-7538(22)00003-1
DOI: https://doi.org/10.1016/j.euromechsol.2022.104506
Reference: EJMSOL 104506

To appear in: *European Journal of Mechanics / A Solids*

Received date : 28 May 2021
Revised date : 7 December 2021
Accepted date : 4 January 2022

Please cite this article as: K. Somlo, B.H. Frodal, C.V. Funch et al., Anisotropic yield surfaces of additively manufactured metals simulated with crystal plasticity. *European Journal of Mechanics / A Solids* (2022), doi: https://doi.org/10.1016/j.euromechsol.2022.104506.

Anisotropic yield surfaces of additively manufactured metals simulated with crystal plasticity

K. Somlo[a], B. H. Frodal[b], C. V. Funch[a], K. Poulios[a], G. Winther[a], O. S. Hopperstad[b], T. Børvik[b], C. F. Niordson[a]

[a]*Department of Mechanical Engineering, Technical University of Denmark, Lyngby, Denmark*
[b]*Structural Impact Laboratory (SIMLab), Department of Structural Engineering, NTNU - Norwegian University of Science and Technology, Trondheim, Norway*

Abstract

The mechanical anisotropy created by additive manufacturing (AM) is not yet fully understood and can depend on many factors, such as powder material, manufacturing technology and printing parameters. In this work, the anisotropic mechanical properties of as-built, laser powder bed fusion (LPBF) austenitic stainless steel 316L and titanium alloy Ti-6Al-4V are investigated through crystal plasticity simulations. Periodic representative volume elements (RVEs) are used that are specific to each material. The RVE for austenitic stainless steel consists of FCC crystals with a crystallographic texture measured by X-ray diffraction. The α' martensite microstructure of Ti-6Al-4V is captured with a multi-scale RVE, including internal lamellar structures, using HCP crystals and a synthetically generated texture. For both materials, the crystal plasticity parameters are calibrated against tensile tests carried out on dog-bone specimens printed in different orientations. The RVEs, calibrated to experiments, are applied in virtual material testing and subjected to multiple load cases to generate the Hill-48 and Yld2004-18p yield surfaces of the materials.

Key words: Yield surface, Crystal plasticity, Anisotropy, Titanium alloy, Stainless steel, Additive manufacturing.

1. Introduction

Metal additive manufacturing (AM) facilitates customisation, flexible, small-scale production and complex, light-weight components, which offer high potential primarily in the aerospace, automobile and biomedical sectors. The unique, cyclic thermal history in the AM process creates a heterogeneous microstructure, which leads to anisotropic mechanical properties. For most of the functional engineering applications, anisotropy is unfavourable and has to be accounted for in stress analysis [1, 2].

The microstructure and the mechanical properties of the most common AM metallic materials, i.e. aluminium, stainless steel and titanium alloys, have been thoroughly investigated. The extensive studies of AM metals are necessary because they are significantly different from traditional cast, rolled and extruded materials. In addition, the powder material, the specific AM technology, the scanning strategy, and the building parameters and direction also have considerable impact on the microstructure and important contributions to the mechanical properties [3–5]. This work focuses on the austenitic stainless steel, 316L, and the most common titanium alloy, Ti-6Al-4V, produced by the laser powder bed fusion (LPBF) process.

It has been clearly demonstrated that the AM of 316L creates a microstructure with elongated columnar grains with the [110] crystallographic direction preferentially being parallel to the building direction (BD) [6, 7]. In most studies, the microstructure is characterised by a single austenitic face centered cubic (FCC) phase [8, 9], although a tiny fraction of the ferrite phase with body centered cubic (BCC) structure has also been reported [10]. The grain size of 10-100 µm allows for local texture measurements with electron backscatter diffraction (EBSD), and also measurements of the bulk texture based on X-ray diffraction (XRD) [10, 11]. In addition to the crystallographic texture, defects such as inclusions and porosities, and the grain aspect ratio in relation to the Hall-Petch effect, have been considered as possible sources of anisotropy [7]. Further factors could be the highly oriented cellular subgrain structures, residual stresses and melt pool boundaries [12]. In the case of Ti-6Al-4V, AM can also lead to columnar grains parallel to the BD, which contain fine martensite platelets at multiple scales with well-defined orientations [13, 14]. However, due to the very fine microstructure, it is difficult to experimentally obtain statistically representative crystal orientation distribution (COD) data. In addition, for LPBF Ti-6Al-4V, most available studies reported a single phase α' hexagonal-closed-packed (HCP) lattice structure with a negligible amount of the β phase [15].

To establish a link between the material microstructure and the macroscopically observed mechanical strength, crystal plasticity has become an essential tool, which enables a detailed description of plastic deformation mechanisms. Due to the same chemical composition, but distinct mechanical properties created by the AM compared to conventional processes, crystal plasticity has recently been applied to various AM materials, such as 316L, Ti-6Al-4V and high-manganese steels [16–18]. The most commonly used crystal plasticity constitutive model is the relatively simple power-law rate-dependent model [19, 20]. More complex, recent models can also capture effects of grain boundaries, such as the Hall-Patch strengthening [21], using length-scale dependent constitutive laws. Regarding the numerical implementation, besides the classic finite element method, fast Fourier transform (FFT) based spectral methods have become popular, due to their high efficiency in solving periodic boundary value problems [22, 23].

At larger scales, the homogenised behaviour of the heterogeneous microstructure of AM metals can be described by a homogeneous elastic-plastic material model, using an anisotropic yield function to govern the plastic behaviour. The anisotropic yield criterion can be determined from crystal plasticity simulations or experiments. Numerous anisotropic yield criteria are available in the current state-of-the-art, using quadratic or non-quadratic yield functions with a different number of adjustable parameters and tailored to specific materials, e.g. steels or aluminium alloys [24–26]. In general, the higher the number of parameters that are present in the applied yield function, the more complex and flexible it is. On the other hand, the calibration of multiple parameters requires extensive experimental testing, which is both expensive and time consuming, especially for AM materials.

Furthermore, even the same AM technology and powder material could require different calibrations depending on the printing parameters and scanning strategy. Therefore, instead of expensive experiments, virtual material testing using representative volume element (RVE) or unit cell simulations can be advantageous [26].

Although crystal plasticity studies of AM materials have received a great deal of attention by the research community, only a limited number of studies have dealt with anisotropy simultaneously with simulations and experiments. Even fewer studies have determined anisotropic yield surfaces for AM materials [7, 27–29]. The present work investigates the anisotropic yield properties of LPBF 316L and Ti-6Al-4V by means of RVE simulations supported by uniaxial tensile experiments. While essential elements of the numerical studies are different for the two materials, such as the grain morphology, the method of texture generation and the crystal structure, the overall methodology of applying crystal plasticity simulations based on RVEs to determine different types of anisotropic yield criteria is the same.

The paper is organised as follows. Firstly, the experimental procedure is presented in Section 2, followed by the constitutive model and numerical framework of crystal plasticity in Section 3. The anisotropic yield criteria are described in Section 4 together with the calibration method based on virtual material tests. Section 5 presents the results in terms of stress-strain curves and yield surfaces, which are discussed in Section 6. Concluding remarks are provided in Section 7.

2. Experimental procedure

2.1. Materials and manufacturing

The commercial LPBF systems SLM280 and SLM500 were used in this study with the AISI 316L and Ti-6Al-4V ELI powder materials from the SLM Solutions Group AG. The Ti-6Al-4V ELI powder material, also referred to as a grade 23 material, had a mean particle diameter of 47 µm, while the AISI 316L powder material had a mean diameter of 34 µm. Chemical compositions of the powders were in the ranges specified by the supplier, and more details can be found in [30, 31]. For both materials, a scanning strategy with parallel stripes was used, with a 67° rotation between subsequent layers as illustrated in Figure 1b. Further relevant build parameters are summarised in Table 1. After printing, stress relief was performed at 550 °C for 2 hours to prevent the specimens from warping upon removal from the build plate.

Table 1: Build parameters

Material	Speed [mm/s]	Power [W]	Hatch distance [mm]	Layer height [mm]
Ti-6Al-4V ELI	1100	350	0.12	0.06
AISI 316L	700	235	0.12	0.05

The specimens were printed in two different orientations with their longest axis perpendicular (horizontal, 90°) and parallel (vertical, 0°) to the BD. To ensure similar surface roughness for the horizontal and vertical specimens, all of them were printed with an over-size of 1 mm. The support structure and the over-size (Figure 1c) were then removed by Electrical Discharge Machining (EDM) to obtain the final cross-section.

2.2. Tensile testing

The tensile tests were carried out with the same testing parameters, set-up and dog-bone specimen geometry for both 316L and Ti-6Al-4V. They were conducted according to the ASTM E8/E8M standard [32] at room temperature on MTS 312.21 100 kN servo-hydraulic testing machine under displacement control mode with a loading rate of 0.05 mm/s. The specimens were clamped with MTS 647 side-loading hydraulic wedges, using 100 bar grip pressure. The longitudinal strain was measured with an Instron extensometer with a gauge length of 12.5 mm, as shown in Figure 1d. The reduced section of the machined tensile bar had a length of 23 mm with a cross-section of 5×6 mm^2 (Figure 1a).

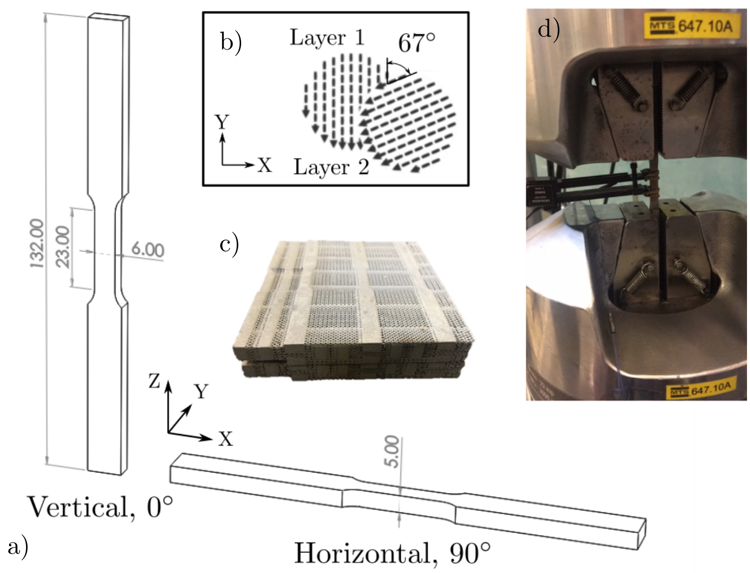

Figure 1: Summary of experimental details: a) Geometry of dog bone specimen printed in different orientations, b) Applied scanning strategy with 67° rotation, c) As-built block of horizontal specimens before EDM, d) Gripped tensile specimen with attached extensometer.

2.3. Microstructure characterisation

In what follows, the methods and results of the material characterisation are summarised. These results are used in the RVE simulations presented in Section 3.3. More details on the microstructure of Ti-6Al-4V and 316L can be found in [30] and [33], respectively. For both materials, light optical microscopy (LOM) was conducted on an Olympus GX41, revealing elongated columnar grains parallel to the building direction, as shown in Figure 2a and c.

The primary grains of Ti-6Al-4V are quite elongated with an aspect ratio of approximately 2, where the longer dimension is in the order of 200 µm. The high cooling rates, in the range 10^3-10^5 K/s, are inherent to the LPBF process and they cause a martensitic α' microstructure for the as-built Ti-6Al-4V [34]. This is in contrast to the two-phase α-β structure commonly reported for cast titanium alloys. The absence of a significant amount of β phase in the tested components has been confirmed through scanning electron microscopy (SEM) and XRD measurements in agreement with other studies of as-built LPBF Ti-6Al-4V [35, 36]. Martensitic structures are obtained at different scales depending on the level of partitioning of the primary grain, leading to so-called primary, secondary and tertiary α' structures, which can be observed in the LOM micrographs in Figure 2b. These hierarchical martensite plates tend to align in mutually orthogonal directions within the same primary grain. The obtained LOM micrographs suggest a preferred orientation of the martensitic plate normals of 55° and 35° with respect to the BD, corresponding to the primary and secondary plates shown in Figure 2b. The result is an average dominant direction of 45°, which is commonly reported for as-built LPBF Ti-6Al-4V [15].

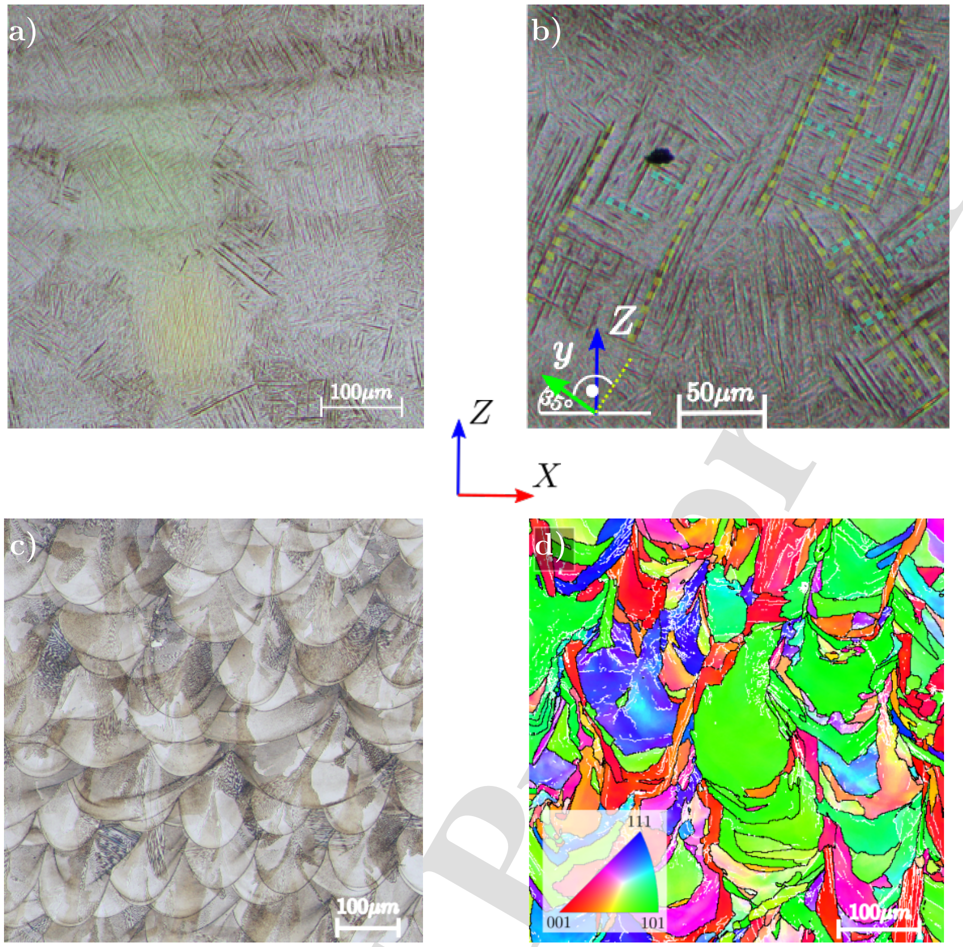

Figure 2: Microstructural characterisation of LPBF metals: a) and b) LOM micrographs of Ti-6Al-4V specimens, c) and d) LOM micrograph and EBSD map of 316L. BD is bottom to top. For the EBSD map, high angle grain boundaries ($> 15°$) are marked in black and low angle grain boundaries (2-15°) in white.The inverse pole figure (IPF) colour code respresents the crystallographic direction of the Z axis.

The LOM micrographs and EBSD maps of 316L reveal a grain aspect ratio of approximately 1.6 and an equivalent grain size of 70 μm, as illustrated in Figure 2c and d. The EBSD measurement was conducted on a Zeiss Supra FEGSEM using an acceleration voltage of 20 kV and an aperture with a 60 μm diameter. The map was acquired with a step size of 1 μm. As shown in the LOM micrographs, the as-built microstructure of the 316L stainless steel consists of elongated austenite grains, semi-circular melt pool boundaries and a hierarchical cellular subgrain structure. This cellular structure is fully austenitic with a potential of slight misorientation with regards to the parent grain as seen in the EBSD map from the low angle grain boundaries within the elongated austenite grains.

The XRD texture analyses were carried out on a Bruker D8 Discovery diffractometer equipped with CrKα radiation. A 0-70° ψ tilt and 0-360° ϕ rotation were applied with a 5° step size and 1.5 s counting time for each combination of tilt and rotation angle. Due to the very fine and hierarchical microstructure of Ti-6Al-4V, statistically representative crystal orientation data by means of XRD could not be achieved, and were thus only obtained for 316L. The pole figures of [111], [200] and [220] reflections of 316L were measured for cross sections with their normal parallel to BD. Considering Figure 3, a preferred alignment of the [220] direction can be observed with respect to the BD. In addition, a 67° rotation between the highest intensity points appears in the texture, particularly for the [111] pole figure, which can be attributed to the effect of the scanning pattern, due to the same 67° rotation between the consecutive layers [30].

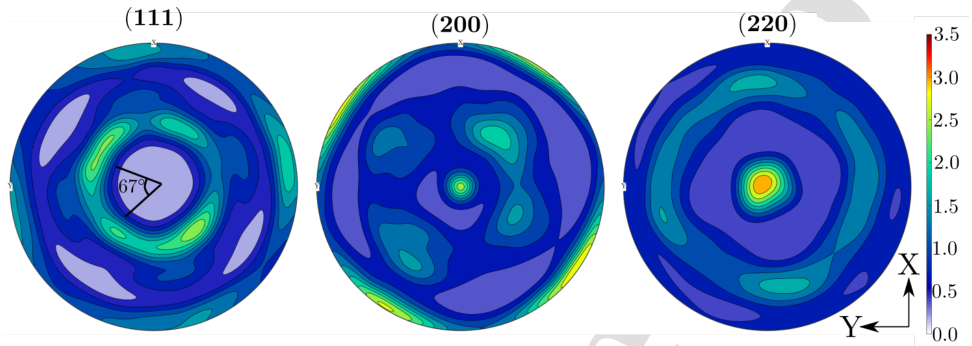

Figure 3: Pole figures of as-built LPBF 316L measured by XRD with BD in the centre of the pole figures [30].

3. Constitutive and numerical modelling of crystal plasticity

In the present section, the single- and polycrystal plasticity models are outlined, which are used for virtual testing of the two investigated AM materials. The main component of the RVE simulations is the crystal plasticity model at the lower scale, including the single crystals with the appropriate slip systems. On the RVE level, besides the single crystal plasticity parameters, the crystallographic texture and grain morphology can also play an important role in the mechanical properties. To determine the macroscopic mechanical behaviour, homogenised quantities are defined, which are directly applied for the generation of anisotropic yield surfaces in Section 4.

3.1. Single crystal plasticity

The crystal plasticity model accounts for infinitesimal elastic deformations and finite plastic deformations; however, it does not include grain boundary strengthening effects. The simulations of this study were carried out using the DAMASK software [23] with the well-established rate-dependent crystal plasticity model from [37]. The kinematics is described by the usual multiplicative decomposition of the deformation gradient

$$\mathbf{F} = \mathbf{F}_e\mathbf{F}_p \tag{1}$$

where $\mathbf{F}_e$ is the elastic part of the deformation gradient, containing the elastic stretching and rigid body rotation of the crystal lattice, and $\mathbf{F}_p$ is the net plastic deformation and rotation, due to shear in multiple slip systems.

The elastic part of the mechanical response of the crystal is based on the Saint Venant-Kirchhoff model [23]

$$\mathbf{S} = \mathbb{C} : (\mathbf{F}_e^T \mathbf{F}_e - \mathbf{I})/2 \tag{2}$$

where $\mathbf{S}$ is the second Piola-Kirchhoff stress and $\mathbb{C}$ is the fourth order elastic stiffness tensor. Utilising the symmetry of the cubic and hexagonal crystals, $\mathbb{C}$ can be reduced to three and five independent elastic constants, respectively. Applying Voigt notation, the elastic coefficients of the 316L FCC crystals are given by C_{11}, C_{12} and C_{44}, while for the Ti-6Al-4V HCP crystals the additional coefficients are C_{13} and C_{33}.

The plastic part of the deformation gradient is obtained by integration of the shear strain rate $\dot{\gamma}^i$ of the different slip systems, contributing to the rate of $\mathbf{F}_p$. For a crystal with N_{sys} slip systems indexed with i, the plastic flow is defined by

$$\dot{\mathbf{F}}_{\text{p}} \mathbf{F}_p^{-1} = \sum_{i=1}^{N_{\text{sys}}} \dot{\gamma}^i \left(\mathbf{s}_{\text{s}}^i \otimes \mathbf{n}_{\text{s}}^i\right) \tag{3}$$

where $\mathbf{s}_{\text{s}}^i$ and $\mathbf{n}_{\text{s}}^i$ are unit vectors along the slip direction and slip plane normal, respectively. The resolved shear stress, τ^i is defined by the Schmid's law:

$$\tau^i = \mathbf{S} \left(\mathbf{s}_{\text{s}}^i \otimes \mathbf{n}_{\text{s}}^i\right) \tag{4}$$

The slip rate is modelled through the phenomenological power law relationship [19], defined by

$$\dot{\gamma}^i = \ \dot{\gamma}_0 \left| \frac{\tau^i}{\tau_c^i} \right|^n \text{sgn}\left(\tau^i\right) \tag{5}$$

where $\dot{\gamma}_0$ is the reference slip rate, n is the power law exponent and τ_c^i is the critical resolved shear stress.

The work-hardening rule is based on an evolution of the slip resistance τ_c^i from a system-dependent initial value τ_0^i to a saturation value τ_∞^i according to the following expression:

$$\dot{\tau_c}^i = h_0 \left(1 + h_{\text{int}}^i\right) \sum_{j=1}^{N_{\text{s}}} \left|\dot{\gamma}^j\right| \left|1 - \frac{\tau_c^j}{\tau_\infty^j}\right|^{a-1} \left(1 - \frac{\tau_c^j}{\tau_\infty^j}\right) h^{ij} \tag{6}$$

where a is the work-hardening exponent, and h_0 is an overall hardening parameter of unit stress. The dimensionless parameters h_{int}^i are slip system specific corrections to h_0. Latent and self hardening are represented by the dimensionless factors h^{ij}, which are typically equal to one for the interaction of a slip system with itself, i.e. $h^{ii} = 1$.

3.2. Constitutive model parameters on the single crystal level

Due to the high cooling rates of the LPBF process, as-built Ti-6Al-4V typically exhibits a purely martensitic α' HCP microstructure [33, 38], while 316L displays elongated austenite grains with FCC crystal structure [30, 39]. Therefore, a single phase material model is assumed for both of the materials, based on the performed X-ray measurements and in agreement with [7, 13]. The crystal plasticity parameters are calibrated against the experimental results, and the identification procedure for Ti-6Al-4V is described in detail in [40]. The same parameter calibration method was conducted for 316L, but was simplified because the FCC crystal has a lower number of elastic and plastic parameters.

Table 2: Elastic constants of the single crystals [40, 41]

Material	Crystal	C_{11}	C_{12}	C_{13}	C_{33}	C_{44}	[GPa]
Ti-6Al-4V	HCP	153.9	87.4	65.5	170.7	47.7	
316L	FCC	198	125			122	

The elastic constants of Ti-6Al-4V are adopted from [42] with a 5% decrease to match the experimental results. A similar fit has been obtained for 316L with the elastic parameters of [43] without any additional scaling. The elastic parameters of both materials are reported in Table 2. The HCP crystal of Ti-6Al-4V includes the basal, prismatic and pyramidal slip systems with relatively high slip resistances, summarised in Table 3.

Table 3: Slip systems and determined initial slip resistance values

		Slip system	Number	τ_0^i [MPa]
Ti-6Al-4V	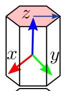	Basal $\langle a \rangle$	3	470
	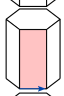	Prismatic $\langle a \rangle$	3	470
	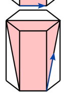	Pyramidal $\langle c + a \rangle$	12	750
316L	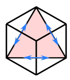	$\{111\}\,\langle 110 \rangle$	12	210

The high slip resistance values are in agreement with recent studies of LPBF Ti-6Al-4V [16, 44], due to their yield strength being superior to conventional titanium alloys. The initial slip resistance of 316L is chosen within the common range from the literature [7, 45] to match the experimentally observed macroscopic yielding.

Table 4 contains all remaining crystal plasticity parameters of both materials, which are required for the simulations. For Ti-6Al-4V a low hardening parameter h_0 is adopted, similarly to [42], because neither self hardening nor softening have been observed.The HCP lattice aspect ratio, c/a, is taken from the literature [38]. The 316L material exhibits substantial hardening and the applied numerical values are in a complete agreement with the work of Charmi et al. [7].

Table 4: Crystal plasticity parameters

Material	n	a	$\dot{\gamma}_0$ [s^{-1}]	c/a	h_0 [MPa]	h^{ij}
Ti-6Al-4V	80	2	0.001	1.587	100	1
316L	20	2.25	0.001	-	300	1 if $i = j$ 1.4 if $i \neq j$

3.3. RVE and texture generation

The crystal plasticity simulations are conducted on periodic, synthetic representative volume elements generated in the DREAM.3D software [46]. For both materials, the RVEs consist of 128×128×128 voxels and account for the observed grain morphology with elongated primary grains along the building direction, i.e. the Z axis, as illustrated in Figure 4a and b. In addition to the grain morphology, the texture is also assumed to be transversely isotropic with respect to the BD for both materials; thus only the corresponding inverse pole figure (IPF) maps are presented in Figure 4c and d. Due to the 67° rotation between the subsequent layers, transverse isotropy is assumed, which is also justified by the LOM and XRD measurements (Figures 2 and 3). Other studies with more detailed experimental investigations also mostly consider the anisotropy perpendicular to the building plane and not in the building plane, independent of the scanning strategy. However, the applied layer rotation with 67° is a better process to ensure isotropy in the XY plane than scanning strategies with e.g. 90° or 45° rotations, because identical scan paths in subsequent layers are avoided [47].

DREAM.3D generates grains of varying size with an equivalent sphere diameter following a normal distribution with a mean value, μ_{ESD}, and a standard deviation, σ_{ESD}. Besides the grain size, the grain aspect ratio can easily be prescribed, which was determined by LOM for both materials (Figure 2).

For the RVE of Ti-6Al-4V the average grain size, μ_{ESD}, has been determined iteratively to obtain a sufficient number of grains for the final RVE using a fixed ratio of $\sigma_{\mathrm{ESD}}/\mu_{\mathrm{ESD}} =$ 0.07. This procedure resulted in an RVE containing 184 elongated primary grains with the prescribed aspect ratio of 2.2. In addition, α' martensite plates are also considered within each primary grain, with a layer thickness approximately 5% of the RVE edge, as shown in Figure 4a. The layered morphology is obtained by post-processing the primary grain morphology, using a simple 3D sine-wave function, as a threshold, to divide each grain into primary and secondary layers. The modified multi-scale RVE still maintains periodicity, which was ensured with appropriate translation of the sine-wave mask of the grains on the surface of the RVE [40]. The layering is based on a prescribed statistical distribution of the layer normal vectors, $\mathbf{n}$, of the grains, reproducing the dominant orientation of the primary α' plates with respect to the building plane. The mean value of this normal distribution is 55° with the standard deviation of 8°.

Regarding the texture, each primary grain contains two mutually orthogonal crystal orientations corresponding to primary and secondary layers, as shown in Figure 4c. In

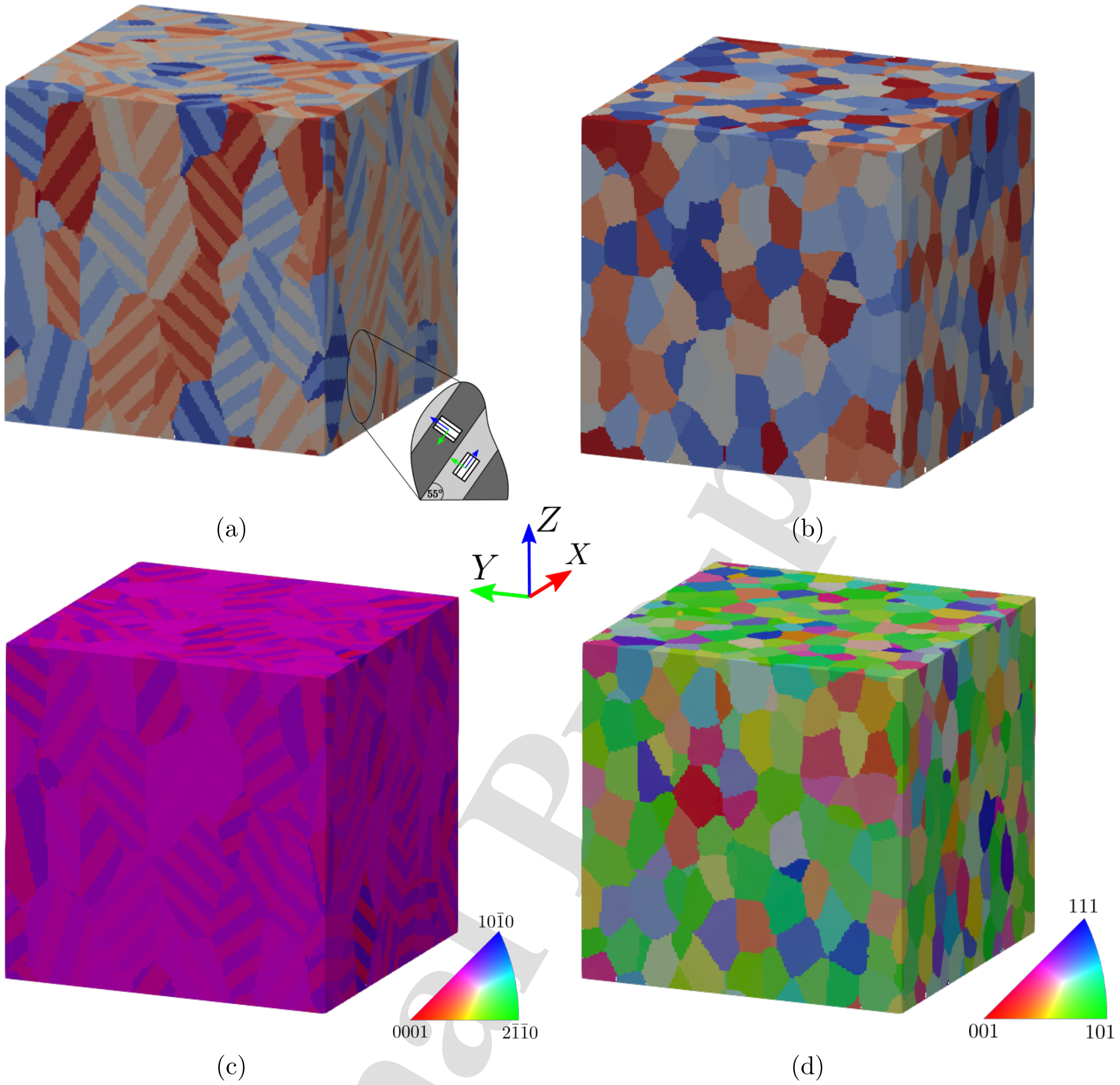

Figure 4: Generated RVEs for (a) Ti-6Al-4V and (b) 316L, (c) synthetic IPF map of Ti-6Al-4V and (d) reconstructed IPF map of 316L with respect to BD

the primary layers, the $[1\bar{1}00]$ direction of the HCP crystal is parallel to $\mathbf{n}$ and the angle between the [0001] direction and the global Z axis is the closest possible to $0°$, as illustrated in Figure 4a. This orientation is rotated $-90°$ around the $[11\bar{2}0]$ direction of the HCP crystal to obtain the orientation of the secondary layers. The ensuing texture is transversely isotropic with the hardest [0001] direction of the HCP crystal having a uniformly random distribution projected onto the XY plane and a preferred alignment perpendicular to the XY plane, as shown in Figure 5. Prior to completing the Ti-6Al-4V RVE applied in this work, mesh convergence studies and case studies with different layer orientations were conducted, see [40] for further details.

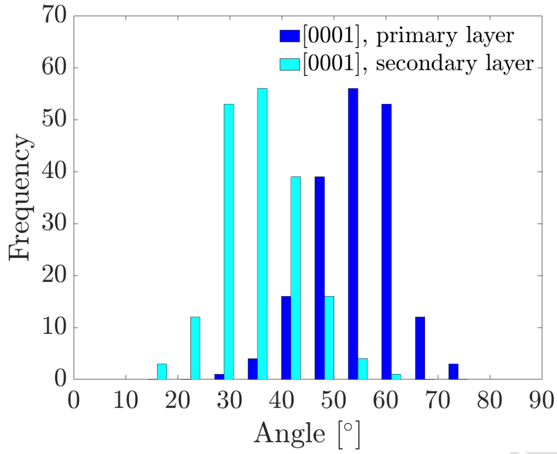

Figure 5: Histograms for the angle between the HCP crystal z axis, i.e. the [0001] direction, and the build plane, i.e. the global XY plane, for the the secondary and primary layers of Ti-6Al-4V [40].

Only primary grains are considered for 316L, since the size of the subgrain dendrite cell structure is two orders of magnitude lower and not visible in the EBSD measurements. The simpler grain morphology of 316L as compared to Ti-6Al-4V, allowed for approximately four times the number of grains in the RVE, namely about 800 grains with an aspect ratio of 1.6. The texture characterised by XRD was employed for generating an RVE with a similar texture. Firstly, the orientation distribution obtained by XRD measurement was reproduced with a representative set of 100 grains. Subsequently, this set of grains was replicated 5 times, with crystal orientations repeatedly rotated by 67° around the Z axis, in order to simulate the printing scan strategy and approximate transverse isotropy. The thereby created bulk texture, including 500 grains, aims at representing the crystal orientations of five consecutive printing layers. Finally, providing this cumulated crystal orientation distribution together with the desired grain size and aspect ratio as input to the DREAM.3D software, the grain tesselation and texture of an RVE were directly obtained. The pole figures of the generated RVE for 316L are shown in Figure 6, and they are in good agreement with the pole figures obtained by XRD (Figure 3).

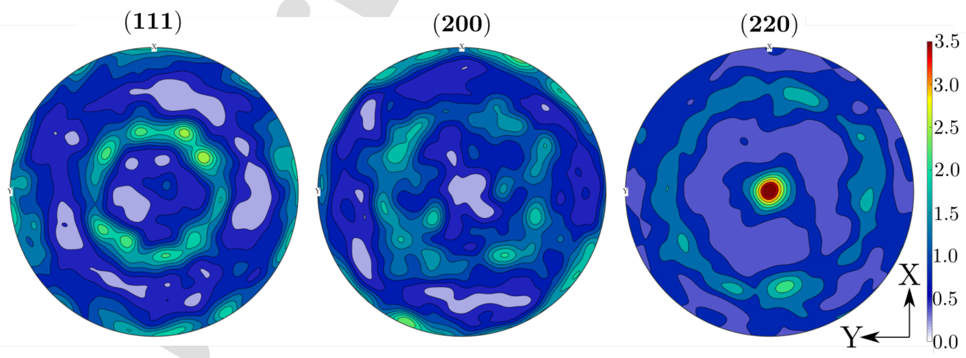

Figure 6: Pole figures [111,200,220] of 316L RVE based on XRD with BD ⊥ to the plane

Considering Figures 2 and 4, assuming transverse isotropy, the primary grain size of both materials is in the order of 100 µm in the build plane. As a result, the RVEs can be considered to have a physical size of 0.7 mm^3 for Ti-6Al-4V and 2.5 mm^3 for 316L. However, length scale effects are not accounted for in the applied crystal plasticity model (Section 3.1), and thus the numerical results are independent of the size of the RVEs.

3.4. RVE homogenisation

To evaluate the macroscopic mechanical properties, homogenised quantities need to be derived from the crystal plasticity simulations of the RVEs. To this end, the homogenised Cauchy stress tensor, $\overline{\boldsymbol{\sigma}}$, deformation gradient, $\overline{\mathbf{F}}$ and plastic power per unit volume, $\overline{\dot{\mathcal{W}}}_{\mathrm{p}}$ are defined as the volume average over all constituents by

$$\overline{\boldsymbol{\sigma}} = \sum_{g=1}^{N_g} v_g \boldsymbol{\sigma}^{(g)}, \quad \overline{\mathbf{F}} = \sum_{g=1}^{N_g} v_g \mathbf{F}^{(g)}, \quad \overline{\dot{\mathcal{W}}}_{\mathrm{p}} = \sum_{g=1}^{N_g} v_g \dot{\mathcal{W}}_{\mathrm{p}}^{(g)} \tag{7}$$

where N_g is the total number of voxels and v_g represents the volume fraction of voxel g. The plastic power per unit volume is determined using the work conjugacy of the plastic Mandel stress, $\mathbf{M}_{\mathrm{p}}^{(g)}$, and the plastic velocity gradient, $\mathbf{L}_{\mathrm{p}}^{(g)}$, at material point g [23]:

$$\dot{\mathcal{W}}_{\mathrm{p}}^{(g)} = \mathbf{M}_{\mathrm{p}}^{(g)} \cdot \mathbf{L}_{\mathrm{p}}^{(g)} \tag{8}$$

4. Phenomenological polycrystal plasticity

In this section, two anisotropic yield criteria, namely the quadratic Hill-48 criterion [24] and the non-quadratic Yld2004-18p criterion [25], are calibrated based on virtual testing using the established RVEs. The calibration procedure adopted in this study is based on the method proposed by Frodal et al. [26]. The aim is to derive yield surfaces that describe the homogenised response at the RVE level.

4.1. Constitutive laws

Plastic yielding at the RVE level can be formulated using the volume-average Cauchy stress tensor and assuming pressure independence as

$$\Phi(\boldsymbol{\sigma}) \equiv \varphi(\boldsymbol{\sigma}) - \sigma_y = 0 \tag{9}$$

where $\varphi(\boldsymbol{\sigma})$ is the equivalent stress, as defined by the applied yield function, and σ_y is the yield stress. The isotropic von Mises yield criterion defines $\varphi(\boldsymbol{\sigma})$ in terms of the deviatoric stress tensor $\mathbf{s}$, by

$$\varphi(\boldsymbol{\sigma}) = \sqrt{\frac{3}{2}\mathbf{s} : \mathbf{s}} \tag{10}$$

where $\mathbf{s}$ is defined as

$$\mathbf{s} = \boldsymbol{\sigma} - \frac{1}{3}\mathrm{tr}(\boldsymbol{\sigma})\mathbf{I} \tag{11}$$

with $\mathbf{I}$ denoting the second order identity tensor.

For anisotropic materials, Barlat et al. [25] proposed to use linear transformations of the deviatoric stress tensor to account for the anisotropy

$$\mathbf{s}' = \mathbf{C}' : \mathbf{s}, \quad \mathbf{s}'' = \mathbf{C}'' : \mathbf{s} \tag{12}$$

where the fourth order tensors $\mathbf{C}'$ and $\mathbf{C}''$ contain the plastic anisotropy coefficients. Assuming an orthotropic material, the matrix form of the linear transformations reads as

$$\begin{bmatrix} s'_{XX} \\ s'_{YY} \\ s'_{ZZ} \\ s'_{XY} \\ s'_{YZ} \\ s'_{ZX} \end{bmatrix} = \begin{bmatrix} 0 & -c'_{12} & -c'_{13} & 0 & 0 & 0 \\ -c'_{21} & 0 & -c'_{23} & 0 & 0 & 0 \\ -c'_{31} & -c'_{32} & 0 & 0 & 0 & 0 \\ 0 & 0 & 0 & c'_{44} & 0 & 0 \\ 0 & 0 & 0 & 0 & c'_{55} & 0 \\ 0 & 0 & 0 & 0 & 0 & c'_{66} \end{bmatrix} \begin{bmatrix} s_{XX} \\ s_{YY} \\ s_{ZZ} \\ s_{XY} \\ s_{YZ} \\ s_{ZX} \end{bmatrix} \tag{13}$$

$$\begin{bmatrix} s''_{XX} \\ s''_{YY} \\ s''_{ZZ} \\ s''_{XY} \\ s''_{YZ} \\ s''_{ZX} \end{bmatrix} = \begin{bmatrix} 0 & -c''_{12} & -c''_{13} & 0 & 0 & 0 \\ -c''_{21} & 0 & -c''_{23} & 0 & 0 & 0 \\ -c''_{31} & -c''_{32} & 0 & 0 & 0 & 0 \\ 0 & 0 & 0 & c''_{44} & 0 & 0 \\ 0 & 0 & 0 & 0 & c''_{55} & 0 \\ 0 & 0 & 0 & 0 & 0 & c''_{66} \end{bmatrix} \begin{bmatrix} s_{XX} \\ s_{YY} \\ s_{ZZ} \\ s_{XY} \\ s_{YZ} \\ s_{ZX} \end{bmatrix} \tag{14}$$

where the stress components are given with respect to the principal axes of anisotropy aligned with the global Cartesian coordinate system XYZ. Among the 18 anisotropy coefficients included in $\mathbf{C}'$ and $\mathbf{C}''$, only 16 are independent [48]. Owing to the microstructure of AM produced materials, transverse isotropy with respect to the XY plane is assumed, as discussed in Section 3.3, and the number of independent parameters can be further reduced to 8 by the symmetry conditions

$$c'_{13} = c'_{23}, \quad c'_{31} = c'_{32}, \quad c'_{12} = c'_{21}, \quad c'_{55} = c'_{66} \tag{15}$$

$$c''_{13} = c''_{23}, \quad c''_{31} = c''_{32}, \quad c''_{12} = c''_{21}, \quad c''_{55} = c''_{66} \tag{16}$$

The equivalent stress defined by the Yld2004-18p yield function of Barlat et al. [25] is given by

$$\varphi(\boldsymbol{\sigma}) = \left(\frac{1}{4} \sum_{k=1}^{3} \sum_{l=1}^{3} |S'_k - S''_l|^a \right)^{\frac{1}{a}} \tag{17}$$

where the exponent a determines the curvature of the yield surface, while S'_k and S''_l are the principal values of the tensors $\mathbf{s}'$ and $\mathbf{s}''$, respectively. Due to the relatively high number of parameters, the Yld2004-18p yield criterion is expected to provide an accurate estimation of the yield surfaces for the AM materials of interest. On the other hand, the yield criterion requires a substantial number of simulations (or physical experiments) to determine the coefficients and it is usually not available in commercial finite element software.

Therefore, besides the rather complex Yld2004-18p yield criterion, the more simple, quadratic Hill-48 yield criterion [24] is also adopted to describe the anisotropic plasticity behaviour, which is defined as

$$\varphi(\boldsymbol{\sigma}) = \sqrt{F\left(\sigma_{YY}-\sigma_{ZZ}\right)^2 + G\left(\sigma_{ZZ}-\sigma_{XX}\right)^2 + H\left(\sigma_{XX}-\sigma_{YY}\right)^2 + 2L\sigma_{YZ}^2 + 2M\sigma_{ZX}^2 + 2N\sigma_{XY}^2} \quad (18)$$

where F, G, H, L, M and N are material parameters. Again, invoking transverse isotropy with respect to the XY plane, the number of parameters can be reduced to four from the two symmetry conditions

$$F = G, \quad L = M \quad (19)$$

4.2. Calibration of yield surfaces

To determine all parameters of the Yld2004-18p yield criterion, usually a large number of experimental tests are required [49, 50]. However, following the procedure proposed by Frodal et al. [26], virtual material testing is performed instead of extensive experimental testing. As a result, the yield surfaces are calibrated based on crystal plasticity simulations with the RVEs described in Sections 3.1 and 3.3. The series of numerical tests to be performed [26] consists of seven uniaxial tension tests in the XZ plane, namely in 15° increments from the X axis to the Z axis, and balanced biaxial tension in the same plane. From these tests, besides the initial yield stresses, the Lankford coefficients are also used for calibration. Further load cases are simple shear tests and uniaxial tension tests at 45° in XY and YZ planes. To obtain high accuracy, plane-strain tension tests are carried out in the XZ plane with loading directions parallel to X and Z axes. In the same plane, a plane-stress balanced biaxial strain test is included, i.e. $\dot{\varepsilon}_{ZZ}/\dot{\varepsilon}_{XX} = 1$. Finally, additional five tests are performed along the X and Z axes with the following strain-rate ratios: $\dot{\varepsilon}_{ZZ}/\dot{\varepsilon}_{XX} = -2.00, -1.57, -1.00, -0.64$ and -0.50.

The uniaxial tension test along the Z axis, aligned with the BD, is considered as a reference load case that is used to normalise the results of all the other test cases. The yield stress of each test is derived from the volume-average Cauchy stress tensor at a volume-average plastic work, derived from Equation (8), corresponding to 0.2% plastic strain in the reference load case. The Lankford coefficient is determined as an average within the 90-100 % range of the plastic work at yielding. The yield surface is calibrated using the method proposed by Frodal et al. [26]. Briefly, the method uses an error function, defined by the normalised volume-average Cauchy stress tensors at yielding, the Lankford coefficients and the equivalent stress, depending on the yield surface parameters c'_{ij}, c''_{ij}, and a, according to Equation (17). These yield surface parameters are determined by means of a global minimisation of the error function, applying the *basin-hopping* algorithm of the SciPy Python package.

The calibration of the Hill-48 yield criterion is based on the same crystal plasticity simulations and volume averaged plastic work as the Yld2004-18p yield surface. However, the calibration requires only four load cases, since the model has only four independent parameters due to the transverse isotropy. Simulations of two uniaxial tensile tests are carried out to determine the coefficients F and H, according to the following equations:

$$F = \frac{1}{2(\sigma^y_{ZZ})^2}, \quad H = \frac{1}{2(\sigma^y_{XX})^2} \tag{20}$$

where σ^y_{ZZ} and σ^y_{XX} are the normal yield stresses in the Z and X directions. In addition, simulations of two shear tests are performed to obtain the coefficients L and N:

$$L = \frac{1}{2(\sigma^y_{YZ})^2}, \quad N = \frac{1}{2(\sigma^y_{XY})^2} \tag{21}$$

where σ^y_{YZ} and σ^y_{XY} are yield stresses in shear with respect to the axes of anisotropy. The parameters of the Hill-48 yield criterion can also be calculated using the Lankford coefficients instead of the yield stresses. However, the yield surfaces calibrated based on the Lankford coefficients gave a poor approximation of the RVE simulations, and are therefore omitted.

5. Results

This section describes the numerical and experimental results, in the same manner for both LPBF manufactured Ti-6Al-4V and 316L. Firstly, the experimental stress-strain curves are presented that serve as the basis for the RVE calibration. Secondly, these calibrations are evaluated by a comparison between simulated and experimental stress-strain curves of dog-bone specimens printed with their axis perpendicular to the BD (90°) and parallel to the BD (0°), respectively. Finally, the obtained Yld2004-18p and Hill-48 yield surfaces of the materials, which are fitted to the yielding points of the RVE simulations, are presented.

5.1. Experimental and numerical uniaxial tension tests

The experimental uniaxial tension tests comprised at least four repetitions for each material and build direction, and the measured stress-strain curves of all of these tests are presented in Figure 7. To determine Young's modulus, E, a linear fit was performed for each stress-strain curve. The range of the fit was $150 - 500$ MPa for Ti-6Al-4V and $50 - 200$ MPa for 316L. The conventional yield points, corresponding to 0.2% plastic strain, were determined by offsetting the fitted lines. The average of these yield points for both materials and build directions are marked in Figure 7. Table 5 summarises all experimentally obtained mechanical properties with their average values and standard deviations.

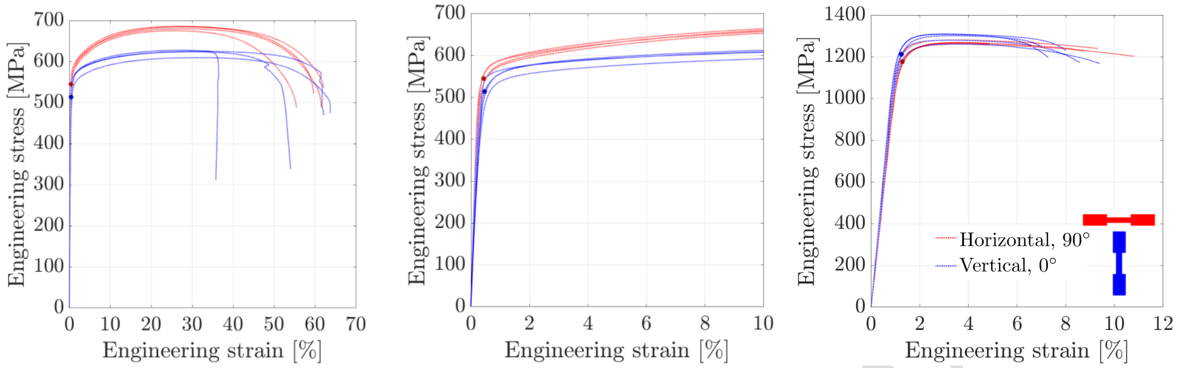

(a) 316L (b) 316L (zoom-in) (c) Ti-6Al-4V

Figure 7: Experimental stress-strain curves for (a,b) 316L and (c) Ti-6Al-4V specimens printed vertically and horizontally, the symbol "$*$" denotes average value of the yield stress σ_y.

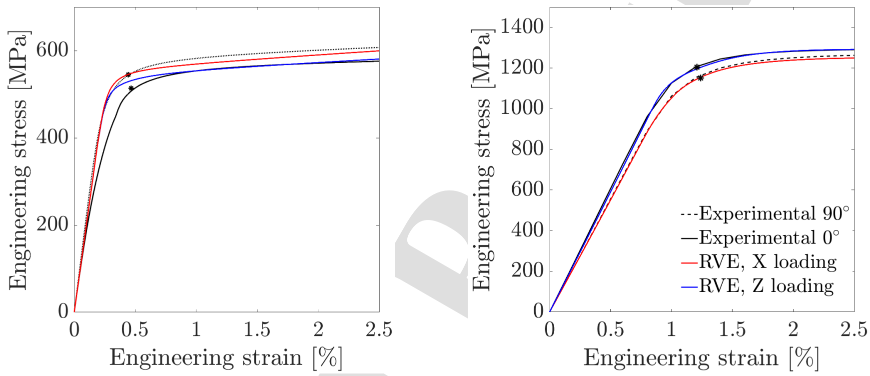

(a) 316L (b) Ti-6Al-4V

Figure 8: Comparison of averaged experimental and numerical stress-strain curves up to an engineering strain of 2.5% for (a) 316L and (b) Ti-6Al-4V, the symbol "$*$" denotes average value of the yield stress σ_y.

The experimental and numerical stress-strain curves are compared in Figure 8. Firstly, using all experimental stress-strain curves, averaged experimental curves were obtained up to 2.5% engineering strain for both materials and loading directions. From the RVE simulations, the volume averaged Cauchy stresses were exported at each strain increment and converted to engineering stresses. The results show that the RVEs of both materials can capture the experimentally observed anisotropic tensile properties with reasonable accuracy. Nevertheless, for the 316L elastic anisotropy could not be obtained by the simulations, and the plastic anisotropy is also slightly underestimated (Figure 8a). The anisotropic yield stresses have opposite ratios for 316L and Ti-6Al-4V, despite the same AM process and scanning strategy being used. LPBF Ti-6Al-4V is stronger along the BD, while LPBF 316L is weaker along the BD, compared to the yield limit in directions parallel to the XY plane. The different anisotropy must primarily stem from the different textures and crystal structures, since length-scale effects are neglected. This finding supports that the manufacturing process with almost identical thermal history creates substantially distinct crystal orientations for the different crystals.

Table 5: Experimental tensile test results of as-built LPBF Ti-6Al-4V and 316L

Material	BD	E [GPa]	σ_y [MPa]	σ_{UTS} [MPa]	$\varepsilon_{\max}$ [%]
Ti-6Al-4V	0°	120.7±6.7	1208±21	1292±18.8	7.6±2.9
	90°	111.6±4.8	1170±12	1258±24.8	8.1±1.0
316L	0°	173.2±28.9	514±20	621±8	53±12
	90°	215.9±11.76	545±12	681±5	59±3

5.2. Evaluation of yield surfaces

In this section, the yield limits of several load cases predicted by the experimentally validated RVEs are used to determine the Hill-48 and Yld2004-18p anisotropic yield surfaces for the two materials. Figure 9 shows for both materials the isolines of the generated Hill-48 and Yld2004-18p yield surfaces in the XZ plane, together with the normalised yield stresses and directions of the plastic flow. The corresponding yield surface parameters are given in Tables 6 and 7.

The different character of the plastic anisotropy of the two materials is illustrated in Figure 10, which shows the normalised yield stresses and Lankford coefficients as functions of the tensile direction in the XZ plane. The RVE simulations (dots) predict minor strength anisotropy for both materials, while the anisotropy in plastic flow, represented by the Lankford coefficient, is substantial with opposite distribution for the two materials.

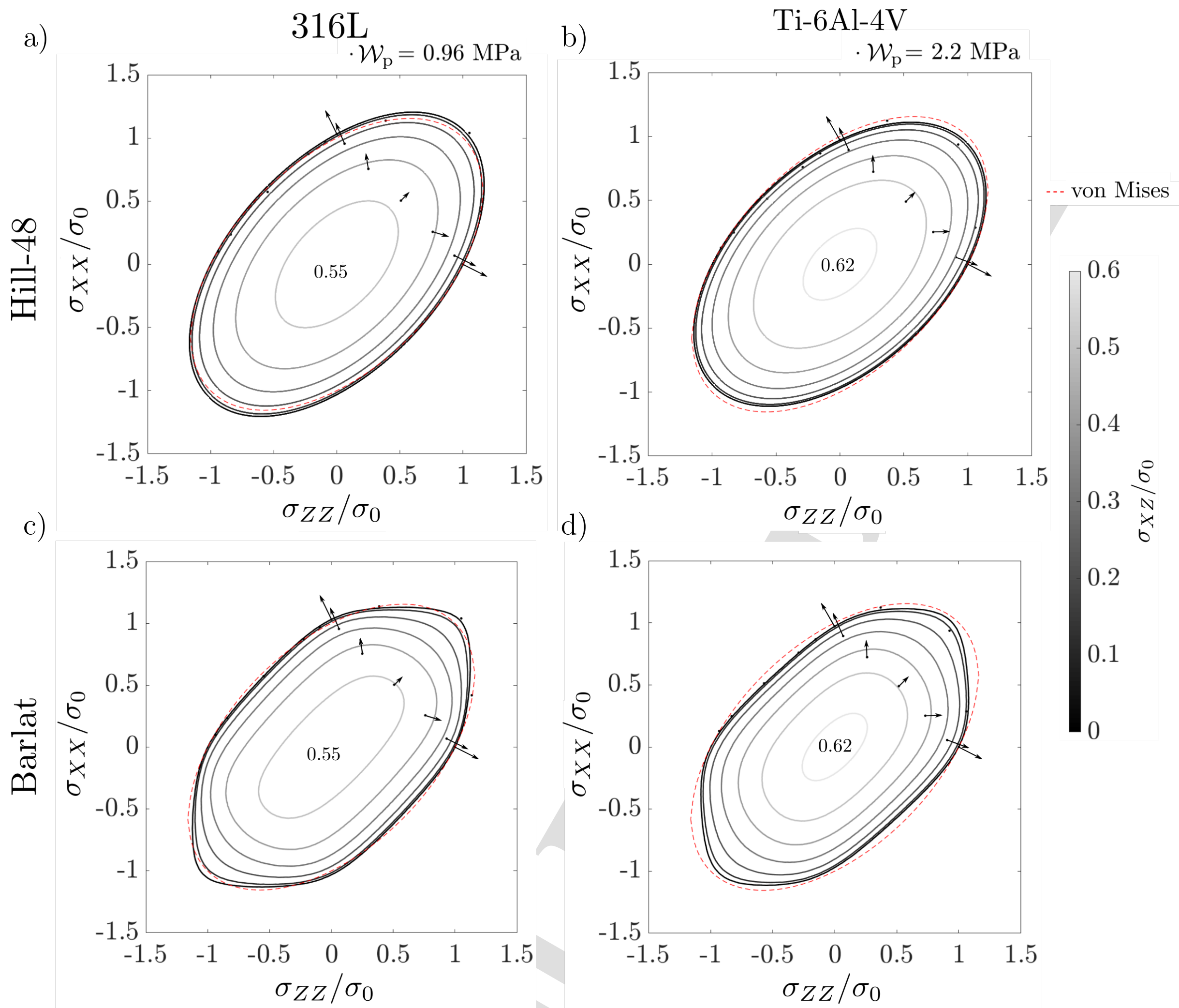

Figure 9: Generated yield surfaces of (a, c) 316L and (b, d) Ti-6Al-4V, projected onto the XZ plane. The reference yield stress σ_0 is taken along the Z axis. Contours of the normalised shear stress σ_{XZ}/σ_0 are plotted in 0.1 increments and the maximum value is shown in the centre. The von Mises yield locus is plotted with a red dashed line.

The results obtained by the fitted yield surfaces show that only the Yld2004-18p yield surface is able to accurately capture the plastic anisotropy predicted in the RVE simulations.

6. Discussion

Considering the experimental results given in Table 5, a significant elastic and plastic anisotropy can be observed for both LPBF 316L and Ti-6Al-4V. Despite using the same manufacturing process, the materials show opposite elastic and plastic anisotropy, which is in agreement with the results reported in the literature [7, 13] and also supported by the crystal plasticity simulations.

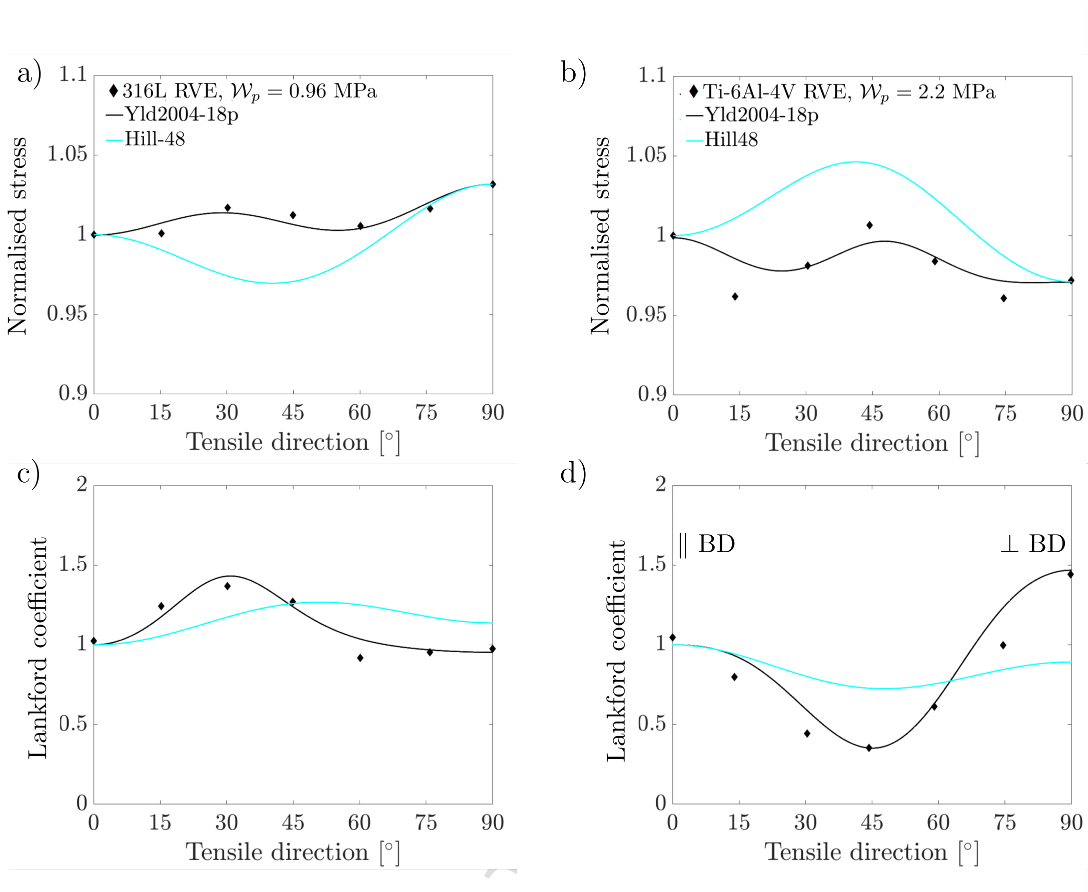

Figure 10: Normalised yield stress and Lankford coefficient from RVE simulations and fitted yield surfaces as function of tensile direction in the XZ plane for (a,c) 316L and (b,d) Ti-6Al-4V, where the 0° direction corresponds to the reference direction taken along the Z axis (∥ BD).

Table 6: Calibrated parameters for the transversely isotropic Hill-48 yield criterion

Parameter	Ti-6Al-4V	316L
$F = G$	0.5	0.5
H	0.56	0.44
$L = M$	1.30	1.65
N	1.47	1.71

Although the RVE for Ti-6Al-4V can precisely reproduce the experimental stress-strain curves (Figure 8b), the number of adjustable parameters in the modelling was much higher than for 316L. One main contributor is the crystal structure because the HCP crystal has a higher number of elastic and plastic parameters than the FCC crystal. In addition, the

Table 7: Calibrated parameters for the transversely isotropic Yld2004-18p yield criterion

Parameter	Ti-6Al-4V	316 L
a	7.97	12.71
$c'_{12} = c'_{21}$	0.6725	0.6821
$c'_{13} = c'_{23}$	1.0714	0.8420
$c'_{31} = c'_{32}$	1.0000	1.0000
c'_{44}	-0.5433	-0.8677
$c'_{55} = c'_{66}$	-1.2553	-1.0821
$c''_{12} = c''_{21}$	1.2785	1.1873
$c''_{13} = c''_{23}$	1.1999	0.8413
$c''_{31} = c''_{32}$	-0.5503	1.0774
c''_{44}	-1.3179	1.0862
$c''_{55} = c''_{66}$	0.4792	-0.8530

texture of Ti-6Al-4V is synthetically generated and the result of a detailed parametric study to achieve the best possible match with the experimental results using commonly reported elastic parameters [40].

In contrast, the crystallographic texture of 316L was obtained from XRD measurements, providing statistically representative data. The crystal plasticity simulations using the measured texture data and the single slip resistance parameter of the FCC crystal can fairly well reproduce the experimental yield points, as shown in Figure 8a. This finding suggests that the texture is the main factor responsible for the plastic anisotropy, which is supported by [7] but in contradiction to [8]. However, the substantial experimentally observed elastic anisotropy, reported in Table 5, could not be captured numerically. Regardless of the applied elastic constants and the software used for simulations, i.e. DAMASK or MTEX [51], the results yield approximately elastic isotropy with the measured texture. The MTEX software provides three different options (Voigt, Hill and Reuss) to estimate the homogenised elasticity tensor for a given texture and elastic constants of the crystal. All three derived elasticity tensors exhibited high elastic stiffness (above 230 GPa) with a minor 2% anisotropy. The computational methods and the related usage of the MTEX software are described in detail in [52].

The source of the elastic anisotropy of LPBF 316L has not been established. Residual strains could play a role in the elastic regime but have not yet been widely reported [6, 8]. In addition, the elastic properties obtained by the performed standard uniaxial tensile tests have arguable accuracy. However, Charmi et al. [7] recently reported similar experimental results confirmed also by simulations, using the same numerical methods as applied in the present study. The difference between the simulated elastic properties of this and the referred study might be explained by different texture data. Namely, the texture determined by local EBSD measurements in [7] is more dominant than the texture of this study obtained by XRD. This hypotheses is justified by the work of Leicht et al. [47], which showed that the texture of specimens built by a scanning strategy with a rotation of 90°, as used by [7], is significantly stronger than with the 67° rotation used in this work. Furthermore, even the experimental yield stresses of [7] show a much stronger anisotropy, approximately 16% compared to the 6% of the present study. This indicates that the scanning strategy does not only effect the crystallographic texture, but also the mechanical anisotropy. Since the simulated plastic anisotropy underestimates the measured one as shown in Figure 8a, an additional conclusion is that other factors such as grain boundaries and precipitates should be accounted for.

Considering Figures 9 and 10, the opposite trends in terms of normalised yield stresses in the 90° direction are clearly visible for 316L and Ti-6Al-4V. Additionally, the shape of the yield surfaces, the maximum shear stresses and the normalised stress at 45° are also different for the two materials. For 316L, the yield stress in the 45° direction is approximately the average of the yield stresses in the 0° and 90° directions (Figure 10a), which is in complete agreement with the result of [7]. The RVE of Ti-6Al-4V predicts the highest yield strength in the 45° direction (Figure 10b), which is also validated experimentally by Agius et al. [13]. Although the corresponding numerical stress-strain curve is not included for brevity, it has been investigated, as the applied synthetic texture has a dominant [0001] alignment at 45° with respect to the BD. It was found that the elastic stiffness in the 45° direction is approximately the average of the stiffness values in the 0° and 90° directions, which is also confirmed by [13]. In addition, preliminary parametric studies showed that the yield stress in the 45° direction can easily be increased even more with higher slip resistance of the pyramidal system, $\tau_{\mathrm{pyr}\langle c+a\rangle}$, without substantially modifying the yield stresses in the 0° or 90° directions. On the other hand, an increased $\tau_{\mathrm{pyr}\langle c+a\rangle}$ leads to a substantial hardening, as commonly reported.

Regarding the performance of the different types of yield surfaces, the Yld2004-18p is obviously superior to the Hill-48 for both materials, due to the higher number of fitted parameters. The constraint of transverse isotropy reduces the independent parameters of Yld2004-18p from 16 to 8, and for Hill-48 from 6 to 4. An important limitation of the quadratic Hill-48 yield criterion is that it cannot account for uniaxial loading in the 45° direction, which is a specific point of interest for AM materials. Furthermore, it also gives a poor estimation of the Lankford coefficients, as shown in Figure 10c and d.

However, considering the AM process and transversely isotropic materials, the Hill-48 criterion is a natural first choice in recent studies [28, 29, 53]. The experimental results and the determined Hill-48 parameters reported in this work are in good agreement with similar investigations of Ti-6Al-4V [28, 29]. Nevertheless, these works lack detailed virtual or experimental material tests to reveal the limitations of the yield criterion. In case of the LPBF 316L, the available literature is more limited to tensile experiments and simulations, and hence a direct comparison of the yield surfaces has not been performed [7, 53]. In these particular cases, the percentage of anisotropy is comparable to the error introduced by the

Hill-48 criterion, which implies that the Hill-48 criterion is not always superior even to a standard isotropic yield criterion. Therefore, it might be a good strategy, depending on the application, either to choose a precise anisotropic yield criterion such as the Yld2004-18p yield criterion, or opt for simplicity and use an isotropic yield criterion. Taking into account the relatively high value of the yield surface exponent, a, of the Yld2004-18p criterion for both materials, the Hershey-Hosford yield criterion [54, 55] seems to be the most appropriate choice among the isotropic yield criteria.

7. Concluding remarks

The anisotropic mechanical properties of laser powder bed fusion (LPBF) austenintic stainless steel 316L and titanium alloy Ti-6Al-4V have been investigated by means of experimental and numerical methods. Crystal plasticity simulations were carried out on RVEs in an attempt to represent the observed microstructural properties such as grain morphology and crystallographic texture. The obtained RVEs are applied to calibrate the Hill-48 and Yld2004-18p anisotropic yield surfaces for the two materials. The main conclusions of this study are summarised as follows:

- Both LPBF 316L and Ti-6Al-4V exhibit elastic and plastic anisotropy but with opposite trends. The 316L material reveals lower strength and stiffness for specimens loaded parallel to the build direction (vertical) and the opposite effect is observed for Ti-6Al-4V, supported by several references [2, 7]. Therefore, our work suggests for specific applications, e.g. quality assurance, that Ti-6Al-4V is preferably tested horizontally and 316L vertically to be conservative.

- Crystal plasticity simulations with RVEs are able to precisely capture the elastic and plastic anisotropy of the various materials. However, this method has limitations with relatively weak crystallographic texture, as demonstrated with the measured texture of 316L. In that case the simulations showed underestimated plastic anisotropy and elastic isotropy.

- The virtual testing of the AM materials reveals a non-quadratic yield surface shape with yield function exponent a considerably larger than 2.

- Considering the shape of the yield surfaces and the thoroughly investigated properties in the 45° direction with respect to the build direction, one has to be careful with the application of the orthotropic Hill-48 criterion. In the present case to precisely capture the anisotropy, the choice of the Yld2004-18p is justified among the two anisotropic models. However, for distinct anisotropy and including the 45° direction for the calibration of the yield surface, the Hill-48 criterion might be acceptable.

- The degree of anisotropy of AM materials highly depends on the printing parameters and scanning strategy. In our particular case with limited anisotropy, the 5% error of the yield stresses introduced by using the von Mises yield function was in the same range as the error of the anisotropic Hill-48 yield function.

It is important to note that with the present numerical model, the experimentally observed plastic anisotropy is attributed to the crystallographic texture for both materials. The RVEs employed account for the observed grain morphology, but they lack an important effect. Using conventional crystal plasticity, they do not include material length scale, thus grain boundary effects are neglected. Despite the minor role of microstructure morphology supported by related studies [7, 42], strain gradient plasticity or dislocation based plasticity could provide further insights. Although the primary grain aspect ratios are similar, the anisotropic properties exhibit opposite trends for the two materials investigated. Therefore, neglecting grain boundary effects seems reasonable for the modelling of Ti-6Al-4V, but not necessarily for 316L.

Acknowledgement

The present research has been conducted in the framework of the AM-LINE 4.0 project, funded by the Innovation Fund Denmark under the grant number 7076-00074B. All specimens were manufactured by one of the project partners, the Danish Technological Institute. BHF, TB and OSH gratefully acknowledge the financial support from NTNU and the Research Council of Norway through the FRINATEK Programme, Project No. 250553 (FractAl).

References

[1] J. J. Lewandowski, M. Seifi, Metal additive manufacturing: A review of mechanical properties, Annual Review of Materials Research 46 (1) (2016) 151–186.

[2] Y. Kok, X. P. Tan, P. Wang, M. L. Nai, N. H. Loh, E. Liu, S. B. Tor, Anisotropy and heterogeneity of microstructure and mechanical properties in metal additive manufacturing: A critical review, Materials and Design 139 (2018) 565–586. doi:10.1016/j.matdes.2017.11.021.

[3] D. Herzog, V. Seyda, E. Wycisk, C. Emmelmann, Additive manufacturing of metals, Acta Materialia 117 (2016) 371–392. doi:10.1016/j.actamat.2016.07.019.

[4] T. M. Mower, M. J. Long, Mechanical behavior of additive manufactured, powder-bed laser-fused materials, Materials Science and Engineering: A 651 (2016) 198–213. doi:10.1016/j.msea.2015.10.068.

[5] E. Liverani, S. Toschi, L. Ceschini, A. Fortunato, Effect of selective laser melting (SLM) process parameters on microstructure and mechanical properties of 316L austenitic stainless steel, Journal of Materials Processing Technology 249 (2017) 255–263. doi:10.1016/j.jmatprotec.2017.05.042.

[6] Y. D. Im, K. H. Kim, K. H. Jung, Y. K. Lee, K. H. Song, Anisotropic mechanical behavior of additive manufactured AISI 316L steel, Metallurgical and Materials Transactions A: Physical Metallurgy and Materials Science 50 (4) (2019) 2014–2021. doi:10.1007/s11661-019-05139-7.

[7] A. Charmi, R. Falkenberg, L. Ávila, G. Mohr, K. Sommer, A. Ulbricht, M. Sprengel, R. Saliwan Neumann, B. Skrotzki, A. Evans, Mechanical anisotropy of additively manufactured stainless steel 316L: An experimental and numerical study, Materials Science and Engineering A 799 (2021) 140154. doi:10.1016/j.msea.2020.140154.

[8] J. M. Jeon, J. M. Park, J. H. Yu, J. G. Kim, Y. Seong, S. H. Park, H. S. Kim, Effects of microstructure and internal defects on mechanical anisotropy and asymmetry of selective laser-melted 316L austenitic stainless steel, Materials Science and Engineering A 763 (2019) 138152. doi:10.1016/j.msea.2019.138152.

[9] A. Röttger, J. Boes, W. Theisen, M. Thiele, C. Esen, A. Edelmann, R. Hellmann, Microstructure and mechanical properties of 316L austenitic stainless steel processed by different SLM devices, International Journal of Advanced Manufacturing Technology 108 (3) (2020) 769–783.

[10] K. Saeidi, X. Gao, Y. Zhong, Z. Shen, Hardened austenite steel with columnar sub-grain structure formed by laser melting, Materials Science and Engineering A 625 (2015) 221–229. doi:10.1016/j.msea.2014.12.018.

[11] M. L. Montero-Sistiaga, M. Godino-Martinez, K. Boschmans, J. P. Kruth, J. Van Humbeeck, K. Vanmeensel, Microstructure evolution of 316L produced by HP-SLM (high power selective laser melting), Additive Manufacturing 23 (2018) 402–410. doi:10.1016/j.addma.2018.08.028.

[12] G. Gray, V. Livescu, P. Rigg, C. Trujillo, C. Cady, S. Chen, J. Carpenter, T. Lienert, S. Fensin, Structure/property (constitutive and spallation response) of additively manufactured 316L stainless steel, Acta Materialia 138 (2017) 140 – 149. doi:10.1016/j.actamat.2017.07.045.

[13] D. Agius, K. I. Kourousis, C. Wallbrink, T. Song, Cyclic plasticity and microstructure of as-built SLM Ti-6Al-4V: The effect of build orientation, Materials Science and Engineering A 701 (2017) 85–100. doi:10.1016/j.msea.2017.06.069.

[14] L. Y. Qin, J. H. Men, L. S. Zhang, S. Zhao, C. F. Li, G. Yang, W. Wang, Microstructure homogenizations of Ti-6Al-4V alloy manufactured by hybrid selective laser melting and laser deposition manufacturing, Materials Science and Engineering A 759 (2019) 404–414. doi:10.1016/j.msea.2019.05.049.

[15] J. Yang, H. Yu, J. Yin, M. Gao, Z. Wang, X. Zeng, Formation and control of martensite in Ti-6Al-4V alloy produced by selective laser melting, Materials & Design 108 (2016) 308 – 318. doi:10.1016/j.matdes.2016.06.117.

[16] D. Zhang, L. Wang, H. Zhang, A. Maldar, G. Zhu, W. Chen, J.-S. Park, J. Wang, X. Zeng, Effect of heat treatment on the tensile behavior of selective laser melted Ti-6Al-4V by in situ X-ray characterization, Acta Materialia 189 (2020) 93–104. doi:10.1016/j.actamat.2020.03.003.

[17] Y. Geng, N. Harrison, Functionally graded bimodal Ti6Al4V fabricated by powder bed fusion additive manufacturing: Crystal plasticity finite element modelling, Materials Science and Engineering A 773 (2020). doi:10.1016/j.msea.2019.138736.

[18] C. Bronkhorst, J. Mayeur, V. Livescu, R. Pokharel, D. Brown, G. Gray, Structural representation of additively manufactured 316L austenitic stainless steel, International Journal of Plasticity 118 (2019) 70 – 86. doi:10.1016/j.ijplas.2019.01.012.

[19] J. Hutchinson, Bounds and self-consistent estimates for creep of polycrystalline materials, Proceedings of the Royal Society of London Series A-mathematical and Physical Sciences 348 (1652) (1976) 101–127. doi:10.1098/rspa.1976.0027.

[20] B. H. Frodal, S. Thomesen, T. Børvik, O. S. Hopperstad, On the coupling of damage and single crystal plasticity for ductile polycrystalline materials, International Journal of Plasticity (2021). doi:10.1016/j.ijplas.2021.102996.

[21] K. Sieradzki, A. Rinaldi, C. Friesen, P. Peralta, Length scales in crystal plasticity, Acta Materialia 54 (17) (2006) 4533–4538. doi:10.1016/j.actamat.2006.05.041.

[22] M. Knezevic, H. F. Al-Harbi, S. R. Kalidindi, Crystal plasticity simulations using discrete fourier transforms, Acta Materialia 57 (6) (2009) 1777–1784. doi:10.1016/j.actamat.2008.12.017.

[23] F. Roters, M. Diehl, P. Shanthraj, P. Eisenlohr, C. Reuber, S. L. Wong, T. Maiti, A. Ebrahimi, T. Hochrainer, H. O. Fabritius, S. Nikolov, M. Friák, N. Fujita, N. Grilli, K. G. Janssens, N. Jia, P. J. Kok, D. Ma, F. Meier, E. Werner, M. Stricker, D. Weygand, D. Raabe, DAMASK – The Düsseldorf Advanced Material Simulation Kit for modeling multi-physics crystal plasticity, thermal, and damage phenomena from the single crystal up to the component scale, Computational Materials Science 158 (2019) 420–478. doi:10.1016/j.commatsci.2018.04.030.

[24] R. Hill, A theory of the yielding and plastic flow of anisotropic metals, Proceedings of the Royal Society of London Series A-mathematical and Physical Sciences 193 (1033) (1948) 281–297.

[25] F. Barlat, H. Aretz, J. W. Yoon, M. E. Karabin, J. C. Brem, R. E. Dick, Linear transfomation-based anisotropic yield functions, International Journal of Plasticity 21 (5) (2005) 1009–1039. doi:10.1016/j.ijplas.2004.06.004.

[26] B. H. Frodal, L. E. B. Dæhli, T. Børvik, O. S. Hopperstad, Modelling and simulation of ductile failure in textured aluminium alloys subjected to compression-tension loading, International Journal of Plasticity 118 (2019) 36 – 69. doi:10.1016/j.ijplas.2019.01.008.
[27] S. A. H. Motaman, F. Roters, C. Haase, Anisotropic polycrystal plasticity due to microstructural heterogeneity: A multi-scale experimental and numerical study on additively manufactured metallic materials, Acta Materialia 185 (2020) 340–369. doi:10.1016/j.actamat.2019.12.003.
[28] D. Agius, C. Wallbrink, K. I. Kourousis, Efficient modelling of the elastoplastic anisotropy of additively manufactured Ti-6Al-4V, Additive Manufacturing 38 (2021) 101826. doi:10.1016/j.addma.2020.101826.
[29] A. E. Wilson-Heid, S. Qin, A. M. Beese, Anisotropic multiaxial plasticity model for laser powder bed fusion additively manufactured Ti-6Al-4V, Materials Science and Engineering A 738 (2018) 90–97. doi:10.1016/j.msea.2018.09.077.
[30] C. V. Funch, T. L. Christiansen, M. A. J. Somers, Effect of edge print parameters on microstructure and high temperature solution nitriding response of additively manufactured austenitic stainless steel, Surface and Coatings Technology 403 (2020) 126385. doi:10.1016/j.surfcoat.2020.126385.
[31] https://www.slm-solutions.com/fileadmin/Content/Powder/MDS/MDS_Ti-Alloy_Ti6Al4V__ELI_0719_EN.pdf.
[32] ASTM E8/E8M-16ae1 standard test methods for tension testing of metallic materials, ASTM international, West Conshohocken, PA (2016). doi:10.1520/E0008_E0008M-16,01.
[33] C. V. Funch, K. Somlo, K. Poulios, S. Mohanty, M. A. J. Somers, T. L. Christiansen, The influence of microstructure on mechanical properties of SLM 3D printed Ti- 6Al-4V, Matec Web of Conferences 321 (2020) 03005. doi:10.1051/matecconf/202032103005.
[34] W. Xu, S. Sun, J. Elambasseril, Q. Liu, M. Brandt, M. Qian, Ti-6Al-4V additively manufactured by selective laser melting with superior mechanical properties, JOM (3) 668–673. doi:10.1007/s11837-015-1297-8.
[35] L. Thijs, F. Verhaeghe, T. Craeghs, J. V. Humbeeck, J. P. Kruth, A study of the microstructural evolution during selective laser melting of Ti-6Al-4V, Acta Materialia 58 (9) (2010) 3303–3312. doi:10.1016/j.actamat.2010.02.004.
[36] H. K. Rafi, N. V. Karthik, H. Gong, T. L. Starr, B. E. Stucker, Microstructures and mechanical properties of Ti6Al4V parts fabricated by selective laser melting and electron beam melting, Journal of Materials Engineering and Performance 22 (12) (2013) 3872–3883. doi:10.1007/s11665-013-0658-0.
[37] D. Peirce, R. Aasaro, A. Needleman, Material rate dependence and localized deformation in crystalline solids, Acta Metallurgica 31 (12) (1983) 1951–1976. doi:10.1016/0001-6160(83)90014-7.
[38] C. Zambaldi, Y. Yang, T. R. Bieler, D. Raabe, Orientation informed nanoindentation of α-titanium: Indentation pileup in hexagonal metals deforming by prismatic slip, Journal of Materials Research 27 (1) (2012) 356–367. doi:10.1557/jmr.2011.334.
[39] K. Saeidi, X. Gao, Y. Zhong, Z. Shen, Hardened austenite steel with columnar sub-grain structure formed by laser melting, Materials Science and Engineering: A 625 (2015) 221 – 229. doi:10.1016/j.msea.2014.12.018.
[40] K. Somlo, K. Poulios, C. Funch, C. Niordson, Anisotropic tensile behaviour of additively manufactured Ti-6Al-4V simulated with crystal plasticity, Mechanics of Materials 162 (2021) 104034. doi:10.1016/j.mechmat.2021.104034.
[41] M. P. Petkov, J. Hu, E. Tarleton, A. C. Cocks, Comparison of self-consistent and crystal plasticity FE approaches for modelling the high-temperature deformation of 316H austenitic stainless steel, International Journal of Solids and Structures 171 (2019) 54–80. doi:10.1016/j.ijsolstr.2019.05.006.
[42] M. Kasemer, M. P. Echlin, J. C. Stinville, T. M. Pollock, P. Dawson, On slip initiation in equiaxed α/β Ti-6Al-4V, Acta Materialia 136 (2017) 288 – 302. doi:10.1016/j.actamat.2017.06.059.
[43] S. Sinha, J. A. Szpunar, N. A. Kiran Kumar, N. P. Gurao, Tensile deformation of 316L austenitic stainless steel using in-situ electron backscatter diffraction and crystal plasticity simulations, Materials Science and Engineering A 637 (2015) 48–55. doi:10.1016/j.msea.2015.04.005.

[44] I. A. Riyad, W. G. Feather, E. Vasilev, R. A. Lebensohn, B. A. McWilliams, A. L. Pilchak, M. Knezevic, Modeling the role of local crystallographic correlations in microstructures of Ti-6Al-4V using a correlated structure visco-plastic self-consistent polycrystal plasticity formulation, Acta Materialia 203 (2021) 116502. doi:10.1016/j.actamat.2020.116502.

[45] X. Lu, J. Zhao, C. Yu, Z. Li, Q. Kan, G. Kang, X. Zhang, Cyclic plasticity of an interstitial high-entropy alloy: experiments, crystal plasticity modeling, and simulations, Journal of the Mechanics and Physics of Solids 142 (2020) 103971. doi:10.1016/j.jmps.2020.103971.

[46] M. A. Groeber, M. A. Jackson, DREAM.3D: A digital representation environment for the analysis of microstructure in 3D, Integrating Materials and Manufacturing Innovation 3 (1) (2014) 56–72. doi:10.1186/2193-9772-3-5.

[47] A. Leicht, C. H. Yu, V. Luzin, U. Klement, E. Hryha, Effect of scan rotation on the microstructure development and mechanical properties of 316L parts produced by laser powder bed fusion, Materials Characterization 163 (2020) 110309. doi:10.1016/j.matchar.2020.110309.

[48] T. van den Boogaard, J. Havinga, A. Belin, F. Barlat, Parameter reduction for the Yld2004-18p yield criterion, International Journal of Material Forming 9 (2) (2016) 175–178. doi:10.1007/s12289-015-1221-3.

[49] F. Grytten, B. Holmedal, O. S. Hopperstad, T. Børvik, Evaluation of identification methods for YLD2004-18p, International Journal of Plasticity 24 (12) (2008) 2248–2277. doi:10.1016/j.ijplas.2007.11.005.

[50] M. Fourmeau, T. Børvik, A. Benallal, O. G. Lademo, O. S. Hopperstad, On the plastic anisotropy of an aluminium alloy and its influence on constrained multiaxial flow, International Journal of Plasticity 27 (12) (2011) 2005–2025. doi:10.1016/j.ijplas.2011.05.017.

[51] F. Bachmann, R. Hielscher, H. Schaeben, Texture Analysis with MTEX – Free and Open Source Software Toolbox, Solid State Phenomena 160 (2010) 63–68. doi:10.4028/www.scientific.net/SSP.160.63.

[52] D. Mainprice, R. Hielscher, H. Schaeben, Calculating anisotropic physical properties from texture data using the mtex open-source package, Geological Society Special Publication 360 (1) (2011) 175–192. doi:10.1144/SP360.10.

[53] M. Kořínek, R. Halama, F. Fojtík, M. Pagáč, J. Krček, D. Krzikalla, R. Kocich, L. Kunčická, Monotonic tension-torsion experiments and FE modeling on notched specimens produced by SLM technology from SS316L, Materials 14 (1) (2021) 33. doi:10.3390/ma14010033.

[54] A. V. Hershey, The plasticity of an isotropic aggregate of anisotropic face-centered cubic crystals, Journal of Applied Mechanics 21 (3) (1954) 241–249.

[55] W. F. Hosford, A Generalized Isotropic Yield Criterion, Journal of Applied Mechanics 39 (2) (1972) 607–609. doi:10.1115/1.3422732.

Highlights

- LPBF 316L and Ti-6Al-4V materials are investigated with crystal plasticity
- Moderate elastic and plastic anisotropy with opposite tendencies for the materials
- Main governing factor of the simulated anisotropy is the crystallographic texture
- RVE simulations for virtual material testing to calibrate anisotropic yield criteria
- Yld2004-18p, Hill-48 and von Mises yield criteria are compared

Declaration of interests

☒ The authors declare that they have no known competing financial interests or personal relationships that could have appeared to influence the work reported in this paper.

☐The authors declare the following financial interests/personal relationships which may be considered as potential competing interests: